Scanning for velocity anomalies in the crust and mantle with diffractions from the core-mantle boundary

Elmer Ruigrok,[1] T. Dylan Mikesell,[2,3] and Kasper van Wijk[2]

[1] A novel method, based on differential arrival times of diffractions from the core-mantle boundary, swiftly scans for seismic velocity anomalies in the crust and mantle below an array of seismometers. The method is applied to data from the USArray and the large-scale structural features in the western United States are resolved. High lateral resolution is achieved, but structure is averaged over depth. As such, this method is complementary to surface-wave and tomographic body-wave methods, where averaging takes place in the lateral sense. Processing and data-volume requirements involved are minimal. Therefore, this method can be applied during the early stages of array deployment, before the necessary data is acquired to obtain accurate inversion images. The quick scanner can be used to identify features of interest, upon which the array could be refined. **Citation:** Ruigrok, E., T. D. Mikesell, and K. van Wijk (2012), Scanning for velocity anomalies in the crust and mantle with diffractions from the core-mantle boundary, *Geophys. Res. Lett.*, *39*, L11301, doi:10.1029/2012GL051443.

1. Introduction

[2] The Earth's velocity model is one-dimensional (1D) only to first order. Lateral variations exist not only in the lithosphere, but also in the transition zone and the lower mantle. These variations were discovered by inverting surface-wave velocity dispersion data [*Knopoff*, 1961], body-wave arrival times [*Aki et al.*, 1977], and a combination of both [*Masters et al.*, 1996]. Although all of these inversion methods have proven valuable, they share one major disadvantage: they require large data volumes and many computing and human analysis hours before a final model is obtained. For example, the velocity model of *Burdick et al.* [2010] requires the inversion of 1,390,000 travel-time residuals.

[3] Here, we consider the use of differential times of P_{diff}, the P-wave diffraction along the core-mantle boundary (CMB). This diffracted arrival has a distinct difference when compared to other body-wave arrivals: ray paths of a core-mantle diffraction do not deviate significantly until at the receiver side (Figure 1). Consequently, arrival-time perturbations measured across an array of receivers can be attributed to receiver-side structure. In the following sections we show that just a few P_{diff} arrivals suffice to identify the major crust and mantle anomalies in the western US, without doing any inversion. We first describe the method, and in subsequent sections apply the method to 1D and 2D distributions of USArray stations.

2. Crosscorrelation Method

[4] We can represent a diffraction due to a unit source at position $\mathbf{x}_S$ recorded at receiver position $\mathbf{x}_A$ in the frequency domain as

$$u(\mathbf{x}_A, \mathbf{x}_S, \omega) = A(\mathbf{x}_A, \mathbf{x}_S, \omega)e^{j\omega(T_{\downarrow A}+T_{\rightarrow A}+T_{\uparrow A})}s(\omega), \qquad (1)$$

where $A(\mathbf{x}_A, \mathbf{x}_S, \omega)$ is an amplitude term that describes the amplitude loss over the travel path, $s(\omega)$ is the source spectrum, j is the imaginary unit and ω is the angular frequency. $T_{\downarrow A}$, $T_{\rightarrow A}$ and $T_{\uparrow A}$ are travel-time segments between the source and diffractor, along the diffractor and between the diffractor and receiver, respectively (Figure 1). A similar expression can be written for this diffraction induced by the same source, but detected at station $\mathbf{x}_B$. If we consider one source and receivers that lie on the same great circle path, as in Figure 1, the ray paths from source to diffractor overlap and we can use the equality $T_{\downarrow A} = T_{\downarrow B}$. Crosscorrelating the diffraction arrivals, using the above equality and neglecting amplitude terms, yields the relationship

$$u(\mathbf{x}_A, \mathbf{x}_S, \omega)^* u(\mathbf{x}_B, \mathbf{x}_S, \omega) \propto e^{j\omega(T_{\rightarrow B}-T_{\rightarrow A}+T_{\uparrow B}-T_{\uparrow A})}|s(\omega)|^2. \qquad (2)$$

The crosscorrelation result is a zero-phase wavelet ($|s(\omega)|^2$) with a maximum occurring at a lag time corresponding to the travel-time difference between both diffractions. Repeating the crosscorrelation between varying receiver positions $\mathbf{x}_B$ and a fixed reference receiver $\mathbf{x}_A$, we estimate the travel-time difference function:

$$tt_A(\mathbf{x}_A, \mathbf{x}_B, \theta) = T_{\rightarrow B} - T_{\rightarrow A} + T_{\uparrow B}(\theta) - T_{\uparrow A}(\theta). \qquad (3)$$

We parametrize the effective illumination by the source using the back-azimuth and ray parameter (θ and p, respectively). If we assume the propagation velocity to be constant along the receiver-side of the diffractor, the source dependence of tt_A is limited to θ, which determines the ray path through the medium at the receiver side. We rewrite equation 3 in terms of p as

$$tt_A(\Delta_{AB}, \theta) = p\Delta_{AB} + dT_{AB}(\theta), \qquad (4)$$

where Δ_{AB} is the epicentral distance between $\mathbf{x}_A$ and $\mathbf{x}_B$. The receiver-side travel-time difference is now expressed in one term: $dT_{AB}(\theta) = T_{\uparrow B}(\theta) - T_{\uparrow A}(\theta)$. When $dT_{AB}(\theta)$ is assumed to be known, equation (4) can be used to estimate p

[1]Department of Geoscience and Engineering, Delft University of Technology, Delft, Netherlands.
[2]Department of Geosciences, Boise State University, Boise, Idaho, USA.
[3]Géoazur, UMR 6526, Université de Nice Sophia-Antipolis, CNRS, Observatoire de la Côte d'Azur, Valbonne, France.

Corresponding author: E. N. Ruigrok, Department of Geoscience and Engineering, Delft University of Technology, Stevinweg 1, 2628 CN Delft, Netherlands. (e.n.ruigrok@tudelft.nl)
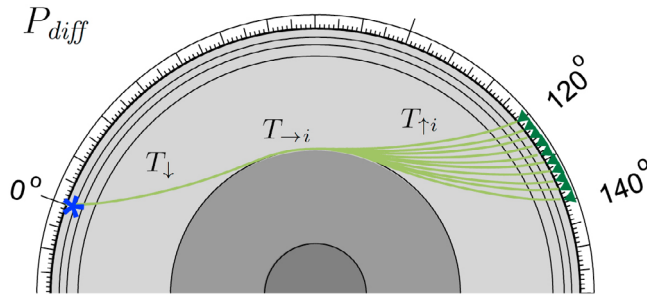
P_{diff}

Figure 1. A cross-section of half the Earth showing P_{diff} arrivals from one source (blue star) and an array of receivers (green triangles). The travel-time segments at the source side, along the diffractor (i.e., core mantle boundary), and at the receiver side are denoted with $T_\downarrow$, $T_{\rightarrow i}$ and $T_{\uparrow i}$, respectively, where i is a receiver index.

[e.g., *Wysession et al.*, 1999; *Mikesell et al.*, 2009]. In this study we take an alternative approach. We assume p to be known and use equation (4) to estimate receiver-side anomalies. Note that p only needs to be known for the CMB-trajectory where the rays deviate (see Figure 1). Therefore, the CMB may strongly vary along parts of the path that overlap. The

signal-to-noise of tt_A can be improved by averaging over multiple inline sources, since tt_A is not a function of the source distance, nor of source depth (equation (4)).

3. Inline Scanning

[5] We apply the anomaly-scanner to a linear sub-array of USArray, shown in Figure 2. The data come from the Mw = 7.4 Simeulue (Indonesia) earthquake, which occurred February 20, 2008. The event and the selected stations lie approximately along the same great circle path, so that the path from the earthquake to the CMB is constant for the entire sub-array. For each station we have the instrument-response function. We remove it from the data by implementing a deconvolution in the frequency domain. Subsequently we band-pass filter the vertical component seismograms between 0.01 and 0.12 Hz; a band in which there is little disturbance from the double-frequency microseism [*Longuet-Higgins*, 1950]. Then we isolate P_{diff} by applying a tapered time-window around the main pulse. The length of this time-window is of the order of the dominant period. Taking a longer time-window would increase the risk of including concurrent phases and reverberations from non-radially symmetric interfaces, which would bias the estimation of the receiver-side anomaly. After isolating P_{diff} we
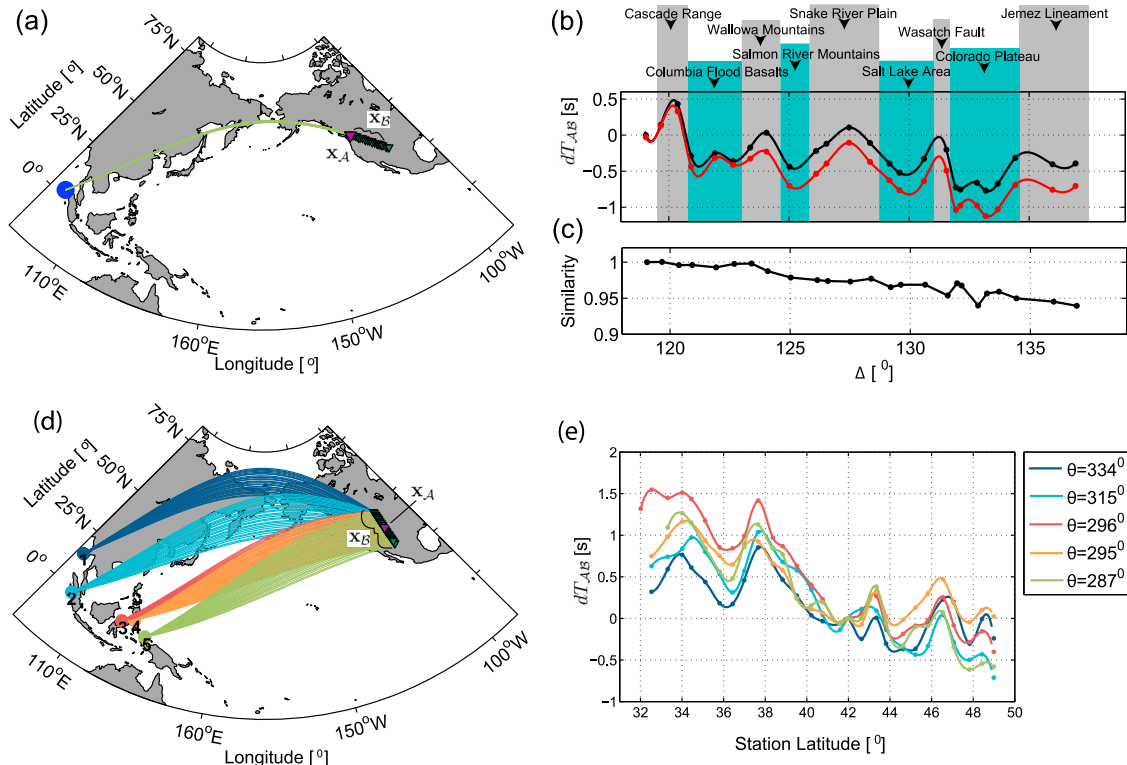

Figure 2. P_{diff} travel-time anomalies for (upper figures) an inline configuration with one earthquake (blue circle) and a line of receivers (green triangles) and (lower figures) multiple earthquakes (colored circles) that are not inline with a line of receivers (i.e., line 21 from the USArray). (a and d) The configurations. (b and e) Correlation of the P_{diff} arrival at a purple reference station with its arrival on all other stations is used to find the P_{diff} travel-time anomalies. Dots represent the extracted anomalies at the different stations, and the lines are created through spline interpolation of these points. In Figure 2b the red and black lines denote the functions with and without a static correction for topography, respectively. (c) The waveform similarity between the P_{diff} arrival at the reference station and all the other stations. On the right-hand side of Figure 2e, the average back-azimuths for the 5 earthquakes are given.

crosscorrelate P_{diff} at the reference station with P_{diff} at all the other stations. From the crosscorrelations we estimate the differential travel-time function (equation (4)), which to first order is a linear function through the origin, with slope p. This feature has been observed for shallower applications in seismology, and termed the "virtual refraction" by *Mikesell et al.* [2009]. We largely remove this linear term by assuming a reference ray parameter of 4. 66 s/deg (Figure S1 in the auxiliary material explains how we found this value), leaving the receiver-side anomaly, $dT_{AB}(\theta)$ (Figure 2b, black line).[1] To eliminate topography as the source of these anomalies, we generate a static correction based on an upper-crustal velocity of 5.8 km/s. Applying the static yields the red line in Figure 2b. This correction shows that topography does lead to a significant time delay, but has little influence on the overall shape of the anomaly.

[6] Equation (2) assumes that the wavelets of P_{diff} at the two receiver locations are identical. However, this wavelet might vary due to propagation effects and the radiation pattern of the source. We check the validity of this assumption by computing the waveform similarity (the maximum amplitude of the crosscorrelation between $\mathbf{x}_A$ and $\mathbf{x}_B$, scaled by the maximum amplitude of the autocorrelation at $\mathbf{x}_A$). A value of one means the effective source wavelets are identical. Figure 2c shows that the similarity is high throughout and only decays slowly from the reference trace, which indicates that the subtle changes in the wavelet of P_{diff} are not the source of the observed anomaly. Instead, travel-time anomalies of Figure 2b correlate with large-scale known features under the receivers. For example, positive anomalies correlate with known elevated temperatures in the crust and mantle, some of which have surface expressions in the form of volcanism. In Figure 2b, the Cascade Range displays a positive anomaly (i.e., decreased velocity), related to active volcanism. Similar correlations can be seen for the Wallowa Mountains and Snake River Plain. Stations near the Wasatch Fault and just north of the Jemez Lineament also show a positive anomaly. Near these stations there are currently no surface expressions of volcanism, but these stations are just north of known volcanic areas. Negative P_{diff} travel-time anomalies are present below the Columbia Flood Basalts and the Colorado Plateau, where subsurface velocities are known to be relatively fast [e.g., *Obrebski et al.*, 2011].

[7] The CMB region below the Pacific is known to be heterogeneous [*Wysession et al.*, 1999]. In Figure 2 we assumed a $p = 4.66$ s/deg to remove the main linear trend in the P_{diff} arrival times. *Wysession et al.* [1999] found values between 4.41 and 4.90 s/deg for raypaths crossing the Pacific. Figure S2 shows the anomaly-function for p values ranging from 4.4 to 4.9 s/deg, with steps of 0.1 s/deg. Realistic structural trends remain only at p values near 4.66 s/deg.

[8] To obtain a measure of the accuracy of the inline scan, we extract the receiver-side anomaly for three more earthquakes. We use the same station array as in Figure 2. These earthquakes are again from the Sumatra region and are therefore still approximately inline with the array. Figure S3 shows the anomaly functions for the individual earthquakes as well as the mean anomaly

---

[1]Auxiliary materials are available in the HTML. doi:10.1029/2012GL051443.

function. The average standard deviation from the mean anomaly function is 0.163 s.

4. Testing for Source-Side Anomalies

[9] The linear configuration underlying equation (4) means that travel-time anomalies can be attributed to the receiver-side. However, this configuration (Figure 2a) is not practical to create a 2D anomaly map. Each line of receivers would require an earthquake – or earthquakes – on the great circle path through the line of receivers, and the results for different lines could not easily be combined to create a single anomaly map. Therefore, we extend the P_{diff} travel-time anomaly scanner to 2D seismic arrays.

[10] When the source and receivers do not lie along the same great-circle path (i.e., in one plane), the source-side ray paths do not overlap, and we need to include the source-side anomaly term:

$$dT_{AB}(\tilde{\theta}) = T_{\downarrow B}(\tilde{\theta}) - T_{\downarrow A}(\tilde{\theta}) + T_{\uparrow B}(\tilde{\theta}) - T_{\uparrow A}(\tilde{\theta}), \qquad (5)$$

where $\tilde{\theta}$ is now an average back-azimuth.

[11] To test the significance of the source-side anomaly term, we select an approximately North-south line of 28 seismic stations from the USArray (Figure 2d). This line crosses various tectonic regions, among others, the eastern edge of the Rocky Mountains. During the time these stations were active (Sept. 2008 to Aug. 2010), numerous P_{diff} arrivals were recorded, especially from earthquakes in Southeast Asia. Due to the large distance traversed by P_{diff} (Δ can be 100–150°), some arrivals have a poor signal-to-noise ratio. Therefore, we only consider five events with Mb > 6.5, with easily identifiable P_{diff} arrivals in the seismic record. The reference station is the purple triangle in Figure 2d, and we apply the same processing as in Section 3 to estimate P_{diff} travel-time anomalies for each of the five earthquakes. Figure 2e displays the travel-time anomalies as a function of station latitude, for the five different earthquakes. Although there are differences between the five functions, the major features (high-amplitude and relatively small wavelength) are common to all. This leads to the conclusion that source-side features and variations in velocity along the CMB are secondary.

[12] Residual linear trends are to be expected among the five events because we know that the lower mantle below the Pacific is heterogeneous [*Wysession et al.*, 1999]. Therefore, it is formally not correct to assume a constant p for each event when removing the linear term in equation (4). The average remaining linear trend in Figure 2e is -0.087 s/deg. The standard deviation σ of this linear trend is 0.028 s/deg. This σ is almost three times as high as for closely located sources (Figure S3). Still, it is only 0.6% of the reference ray parameter (4.66 s/deg), indicating that there is – on average – little velocity variation over the different CMB paths as depicted on Figure 2d.

[13] In summary, even though there are some differences in trend and local P_{diff} travel times, generally the same travel-time anomalies are recovered in Figure 2e for each of the five events. Therefore, the influence of source-side velocity anomalies in equation (5) turns out to be small with respect to the receiver-side anomalies. A positive velocity anomaly in the South is correlated to unstable Proterozoic terranes and a negative velocity anomaly in the North is the
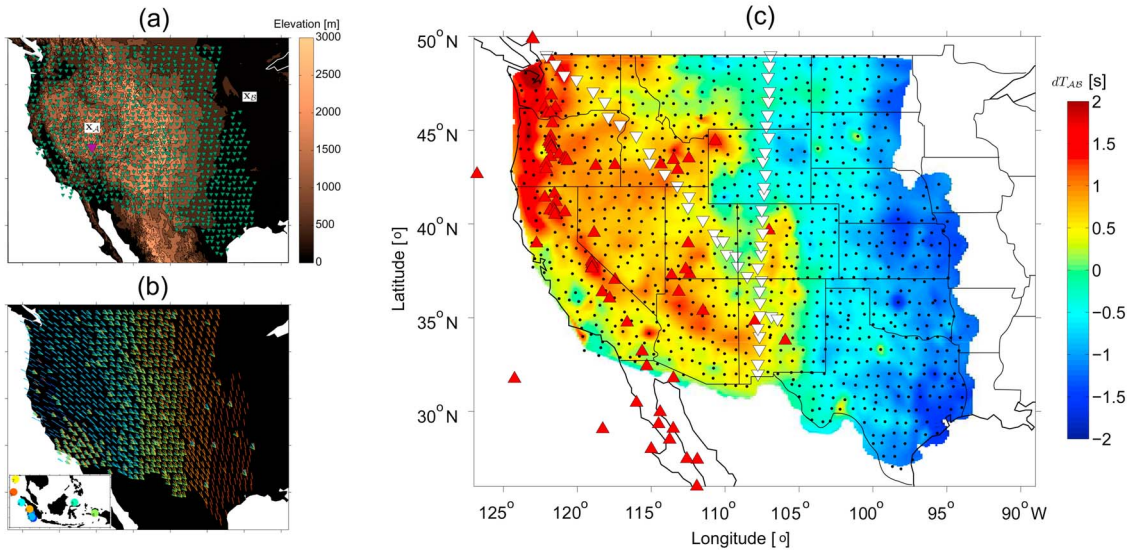
Figure 3. (a) The location of USArray stations used in this study (green triangles) projected onto a topographic map of part of the USA. The reference station at position $\mathbf{x}_\mathcal{A}$ is indicated by the purple triangle. (b) Illumination map – the colored lines denote the back-azimuth to the earthquakes, and these correspond to the colors of the circles in the inset (Indonesian Archipelago). (c) P_{diff} travel-time anomaly map, combined with 1) the primarily Holocene volcanism (red triangles, source: http://www.volcano.si.edu/); 2) USArray stations used in this study (black dots); 3) the station locations used in Figures 2a–2c (NE-SW subarray of white triangles) and Figures 2d and 2e (N-S subarray of white triangles).

result of a stable Archean lithosphere. Superposed on these large features are smaller-scale travel-time perturbations common to all five earthquakes, but difficult to correlate with known features using just one line. In the following section, we neglect the source term in equation (5) and image receiver-side anomalies in a 2D sense.

5. Map Scanning

[14] Since 2006 USArray seismic stations have covered a large part of the USA. Most stations are moving from the West to the East in a roll-along fashion (the transportable array), see *Levander et al.* [1999]. Simultaneously, there is a reference network consisting of permanent stations. We use data from September of 2007 to June of 2010 to image receiver-side anomalies from the West Coast to the Great Plains. The distribution of stations used in this study is depicted in Figure 3a. The permanent and quiescent station TA.R11A in Nevada ($\mathbf{x}_\mathcal{A} = 38.3489°N, 115.5854°W$) is used as the reference station to scan for heterogeneity in the crust and mantle using the P_{diff} arrival from nine earthquakes with Mb > 6.5. These events occurred around the Indonesian Archipelago (Figure 3b, inset) such that most of the great-circle paths cross Alaska. Hence, the contiguous USArray stations are illuminated with a back-azimuth close to NW, as shown in Figure 3b. On the same figure, swaths of North-south stations that were simultaneously active for a given event can be recognized. We select a total of 4076 arrival times for 993 different stations. Thus, each station is illuminated on average by ~4 events.

[15] For each event in Figure 3b (inset), we cross-correlate the windowed P_{diff} arrival at $\mathbf{x}_\mathcal{A}$ with all other available stations. We extract the differential travel-time function and remove the linear term to isolate the receiver-side travel-time anomaly $dT_{\mathcal{AB}}(\tilde{\theta})$. To remove the linear term we use a fixed

ray parameter $p = 4.66$ s/deg (equation (4)). We average the travel-time anomalies at each station over the available events to suppress non-stationary noise. A static correction is applied in the same way as the example in Section 3. Finally, we remove the mean from the entire 2D anomaly function (1.12 s is added) and perform a bi-cubic interpolation, resulting in the anomaly map of Figure 3c.

[16] The receiver-side anomaly map is an integration over the entire ray path from the CMB to the Earth's surface. This path is more than 3000 km long. However, the largest heterogeneity is expected near the Earth's surface, where rays converge onto the stations. To first order, the anomaly map shows similar features to those from travel-time or velocity inversion models of the western USA [e.g., *Schmandt and Humphreys*, 2010; *Burdick et al.*, 2010; *Obrebski et al.*, 2011; *Ritzwoller et al.*, 2011]. Slow velocities (positive travel-time anomalies) in the west are related to magmato-tectonic activity while high velocities (negative travel-time anomalies) in the east are related to stable Archean lithosphere. The slowest anomalies correlate well with Cenozoic volcanic activity (red triangles in Figure 3c). Positive travel-time anomalies below South-Dakota and Texas are likely related to thick sedimentary packages, where the extra time lag through the sediments is not compensated by a thinner crust. Figure S4 compares our results with a recent inversion model by *Obrebski et al.* [2011].

6. Discussion

[17] This new method resembles P- and S-wave residual mapping [e.g., *Dziewonski and Anderson*, 1983; *Martynov et al.*, 2004]; however, rather than comparing the observed arrival time at $\mathbf{x}_\mathcal{B}$ with a synthetic arrival at $\mathbf{x}_\mathcal{B}$, we compare the relative arrival time between $\mathbf{x}_\mathcal{A}$ and $\mathbf{x}_\mathcal{B}$, after a correction for the differential CMB path. When looking at

lateral structure, the main advantage to our method is that our results are data driven. A good estimate of the CMB velocity is required, but it can be directly obtained from the data. Residual mapping depends on an accurate source location and velocity model to derive synthetics. Errors in either of these will propagate into the mapped residuals. Figure S5 compares raypath characteristics of the P_{diff}-phase that we use to the P-phase used in residual mapping.

[18] Data processing is limited to removing the instrument response, time-windowing around the P_{diff} arrival, low-pass filtering below microseism disturbances, and cross-correlation to extract the differential arrival times. Removing the instrument-response is a vital step because near the low end of the frequency band we use, USArray stations can have phase differences exceeding 10 deg. These phase delays may be on the same order as the delays caused by receiver-side structure and therefore need to be corrected.

[19] Our results illustrate the benefit of adding global-phases for tomographic inversion to improve lateral resolution of subsurface images. In tomography, travel-time perturbations are smeared along the entire ray path. Incorporating receiver-side information from the swift P_{diff} anomaly scanner may serve to establish lateral resolution with greater confidence. Furthermore, S_{diff} can be used instead of P_{diff} to swiftly scan S-wave anomalies. This methodology could also be applied to P_n or S_n to scan specifically for crustal anomalies, establishing better constraints on depth.

[20] The main advantage of the new method lies in its speed and simplicity. The anomaly scanner is especially useful to identify features that deserve a more expensive inversion and a denser seismic array. The quality of the extracted features depends directly on the data signal-to-noise ratio and the GPS clock accuracy at each station. In the frequency band used, the noise is primarily caused by the single-frequency microseism. Since this noise is non-stationary, we suppress its influence by averaging travel-time anomaly functions from many events with similar back-azimuths.

[21] We found that no small-wavelength features are introduced in the travel-time anomaly when different CMB paths are used (see Figures 2d, 2e, S1, and S3). This means that small-scale CMB heterogeneity, if present, does not map into the differential travel times. The long-wavelength character of the anomaly function, however, does change when different CMB paths are considered. This wave-number separation between receiver-side and CMB imprints creates the possibility for a simultaneous inversion. One could invert for a CMB structure for which the travel-time anomalies from different CMB trajectories would optimally overlap, as in Figure 2e. In this way, one could simultaneously estimate a CMB model while improving the absolute amplitudes of the receiver-side anomaly map.

7. Conclusion

[22] We identified velocity anomalies in the crust and mantle under a linear array of receivers from differential P_{diff}

arrivals from earthquakes inline with the receivers. Using just one earthquake, clear receiver-side structure is resolved. We confirmed the stability of the scan by using a set of nearby earthquakes. We extended the method to earthquakes not inline with the receivers. This extension proved valid as source-side and CMB structure resulted in only small variations in the mapped anomalies. This allowed us to apply the scan to a regional grid of receivers across the western half of contiguous USA. By averaging the results from 9 different earthquakes, we created a 2D map of the receiver-side structure. Strong correlation with known features under the western half of the USA confirmed the validity of this fast and robust technique. P_{diff} travel-time anomalies are capable of high lateral resolution under the receivers, but average in the vertical direction. Therefore, the method is complementary to surface- and body-wave tomography, where averaging takes place in the lateral sense.

References

Aki, K., A. Christoffersson, and E. S. Husebye (1977), Determination of the three-dimensional seismic structure of the lithosphere, *J. Geophys. Res.*, *82*(2), 277–296.
Burdick, S., et al. (2010), Model update 2010: Upper mantle heterogeneity beneath North America from travel time tomography with gobal and USArray Transportable Array data, *Seismol. Rev. Lett.*, *81*, 689–693.
Dziewonski, A. M., and D. L. Anderson (1983), Travel times and station corrections for P waves at teleseismic distances, *J. Geophys. Res.*, *88*(B4), 3295–3314.
Knopoff, L. (1961), Green's function for eigenvalue problems and the inversion of Love wave dispersion data, *Geophys. J. Int.*, *4*, 161–173.
Levander, A., E. D. Humphreys, G. Ekstrom, A. S. Meltzer, and P. M. Shearer (1999), Proposed project would give unprecedented look under North America, *Eos Trans. AGU*, *80*(22), 245.
Longuet-Higgins, M. (1950), A theory of the origin of microseisms, *Philos. Trans. R. Soc. London. Ser. A*, *243*, 1–35.
Martynov, V., F. Vernon, D. Kilb, and S. Roecker (2004), Directional variations in travel-time residuals of teleseismic P waves in the crust and mantle beneath Northern Tien Shan, *Bull. Seismol. Soc. Am.*, *94*(2), 650–664.
Masters, G., S. Johnson, G. Laske, and H. Bolton (1996), A shear-velocity model of the mantle, *Philos. Trans. Math. Phys. Eng. Sci.*, *354*, 1385–1411.
Mikesell, D., K. van Wijk, A. Calvert, and M. Haney (2009), The virtual refraction: Useful spurious energy in seismic interferometry, *Geophysics*, *74*(3), A13–A17.
Obrebski, M., R. Allen, F. Pollitz, and S.-H. Hung (2011), Lithosphere-asthenosphere interaction beneath the western United States from the joint inversion of body-wave traveltimes and surface-wave phase velocities, *Geophys. J. Int.*, *185*, 1003–1021.
Ritzwoller, M., F.-C. Lin, and W. Shen (2011), Ambient noise tomography with a large seismic array, *C. R. Geosci.*, *343*, 558–570.
Schmandt, B., and E. Humphreys (2010), Complex subduction and small-scale convection revealed by body-wave tomography of the western United States, *Earth Planet. Sci. Lett.*, *297*, 435–445.
Wysession, M., A. Langenhorst, M. Fouch, K. F. G. Al-Eqabi, P. Shore, and T. Clarke (1999), Lateral variations in compressional/shear velocities at the base of the mantle, *Science*, *284*, 120–125.